

Physical device modeling of carbon nanotube/GaAs photovoltaic cells

Hong Li, Wan Khai Loke, Qing Zhang,^{a)} and S. F. Yoon

Microelectronics Center, School of Electrical and Electronics Engineering, Nanyang Technological University, S1-B2c-20, Singapore 639798, Singapore

(Received 16 November 2009; accepted 23 December 2009; published online 25 January 2010)

Photovoltaic response from semiconducting single-walled carbon nanotubes/n-type GaAs heterojunctions has been investigated. We propose a detailed device model of the photovoltaic cell, in which electron transport can be described as follows. The thermionic emission and tunneling through the spike barrier caused by the conduction band discontinuity dominate electron transport under a low and high-forward bias, respectively. In contrast, the dominant transport mechanisms at low and high-reverse bias could be attributed to the direct and Fowler–Nordheim tunneling through a molecular junction, respectively. Within this framework, the current-voltage characteristics of the photovoltaic response can be quantitatively described. © 2010 American Institute of Physics. [doi:10.1063/1.3293452]

In order to utilize the unique electronic properties of carbon nanotubes (CNTs) in the present semiconductor technology, many groups have attempted to incorporate CNTs into conventional bulk semiconductors.^{1–3} One of the promising applications is CNT/III–V semiconductor hybrid devices as both CNTs and III–V semiconductors have many superior electrical and optical properties. For instance, due to the one-dimensional nature of CNTs, electron transport in CNTs can be ballistic over a micrometer scale.⁴ Field-effect hole mobility as high as 79 000 cm²/V s has been experimentally observed.⁵ While, GaAs has been widely used in high-speed transistors owing to its high electron mobility.⁶ Thus, from the electrical application point of view, CNT/GaAs hybrid devices could be useful in the areas of high-speed computation and communication. Moreover, CNT/GaAs hybrid devices could have excellent optoelectronic properties as both materials are direct band gap semiconductors. The diameter-dependent band gap of a semiconducting single-walled carbon nanotube (SWNT) can be controlled through growth conditions.^{7,8} Then, the wavelength-dependent sensitivity, depending on the band gap of a semiconducting SWNT, can be chosen continuously from ~0 to 2 eV.⁹ Thus, solar cells constructed from GaAs and SWNT thin film could efficiently absorb light energy with a wide absorption spectrum. Liang and Roth¹⁰ demonstrated diode behavior and photovoltaic (PV) response in CNT/GaAs heterojunctions. Although the CNT/GaAs interface has been studied,¹⁰ the conduction mechanism and device model for CNT/GaAs heterojunctions are still under investigation. In this report, we present a detailed physical model of SWNT/GaAs PV cells.

The sample preparation began with an n-type GaAs substrate capped by a Si₃N₄ layer. A back-contact G that formed an Ohmic contact to the GaAs substrate was deposited. The Si₃N₄ layer in the trench was removed using dry etching between a pair of electrodes S and D (Ti/Au) fabricated on the Si₃N₄ layer. A semiconducting SWNT was placed across the trench and bridged S and D using ac dielectrophoresis technique.^{11,12} The Au/SWNT contact resistances at the S and D electrodes were comparable, around 6 MΩ. Thus a

CNT field-effect transistor (CNTFET) was formed with the SWNT as the channel, the gallium oxide film (formed during dry etching) as the gate dielectric, and the GaAs substrate as the gate electrode [Fig. 1(a)]. The transfer characteristic [see Fig. 1(b)] of the CNTFET shows that the conduction is ambipolar with stronger p-type.

In order to make the SWNT in contact with GaAs, the gallium oxide layer was removed by soaking the device in HCl solution again. As shown in Fig. 2(a), the junction shows a current (I_{DG}) rectification behavior under different bias voltage (V_{DG}) polarities. Figure 2(b) presents the slopes of the linear portion of the $\log I_{DG}-V_{DG}$ curves, i.e., $S = \Delta \log I_{DG} / \Delta V_{DG}$, under a forward bias (FB), i.e., D is biased positively with respect to G ($V_{DG} > 0$), and a reverse bias (RB), respectively. The slope under a low FB ($V_{DG} < 1.1$ V) decreases significantly from 7 dec/V at 50 K to 4 dec/V at 300 K (red open squares), while the slope under a RB remains almost unchanged around 3 dec/V (blue open circles). In contrast, the slope under a high FB ($V_{DG} > 1.1$ V) decreases slightly from 2.8 dec/V at 50 K to 1.4 dec/V at 300 K (red open diamonds). In a semiconductor heterojunction, the thermionic emission current component is temperature-dependent, while, the tunneling current component does not show significant temperature dependence.¹³ Thus, we suggest that the tunneling and thermionic emission dominate the RB and low FB cases, respectively. Under the

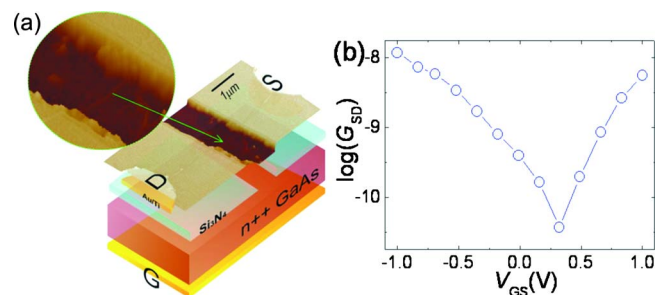


FIG. 1. (Color online) (a) An atomic force microscopy image of a typical device. “G,” “S,” and “D” represent the gate, source, and drain electrodes, respectively. The green arrow delineates the SWNT-channel. (b) Logarithm of SWNT-channel conductance [$\log(G_{SD})$] vs gate voltage (V_{GS}).

^{a)}Electronic mail: eqzhang@ntu.edu.sg.

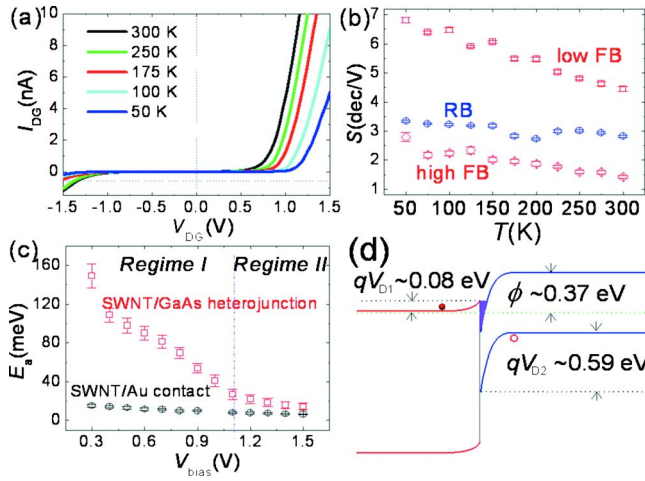


FIG. 2. (Color online) (a) I_{DG} vs V_{DG} curves from 50 to 300 K. (b) slope of the linear portion of $\log I_{DG}$ vs V_{DG} curves at different temperatures at the low FB (red open squares), high FB (red open diamonds) and RB (blue open circles), respectively. (c) V_{bias} -dependent activation energies (E_a) of the SWNT/GaAs heterojunction (red open squares) and the SWNT/Au contact (black open circles), respectively. (d) Schematic energy band diagram of the SWNT/GaAs heterojunction. The purple area delineates the inversion layer.

high FB, tunneling may play a major role, rather than thermionic emission.

The activation energy E_a associated with the thermionic emission process ($I_{DG} \propto \exp(-qE_a/kT)$, where q is the elementary charge and k is the Boltzmann constant) as a function of the FB voltages can be estimated from the Arrhenius plot.¹⁴ As shown in Fig. 2(c), two different regimes (I and II) with the ‘boundary’ located at $V_{bias} \sim 1.1$ V are seen (red open squares). In regime I, E_a continuously decreases when the FB increases. Positive V_{DG} partially counterbalances the built-in potential, and hence reduces the energy barrier for thermionic emission. In contrast, E_a varies negligibly in regime II because tunneling current sets in and then plays a dominant role, leading to “effective” E_a less sensitive to V_{DG} bias.¹⁵ E_a was also extracted from the temperature-dependent I_{DS} for the SWNT/Au contact, as illustrated in Fig. 2(c) (black open circles).¹⁵ It is noted that E_a values are much smaller (up to ten times) than those of the SWNT/GaAs barriers (red open squares). It suggests that the effects of the SWNT/Au contact barrier on I_{DS} are negligible, and thus I_{DG} – V_{DG} characteristics reveal the intrinsic properties of the SWNT/GaAs p-n heterojunction.

The energy band alignment of the device in thermal equilibrium condition is constructed in Fig. 2(d). Under a low FB, thermionic emission is the dominant transport mechanism, and the bias voltage effectively varies the barrier height. The current can be expressed as¹⁶

$$I_{DG} = A \exp[-q(V_D - \Delta E_c)/kT] \{ \exp[q(V_{DG} - I_{DG}R_{ct})/nkT] \}, \quad (1)$$

where A is a temperature-dependent parameter related to the fraction of those electrons having sufficient energy to overcome the activation energy barrier and actually do so.¹⁶ V_D is the total built-in potential. $q\Delta E_c \approx 0.3$ eV is the conduction band (CB) discontinuity between GaAs and SWNT.^{17,18} R_{ct} is the Au/SWNT contact resistance. n is a temperature-dependent ideality factor.

Through fitting Eq. (1) to the measured I_{DG} – V_{DG} curves, we have $V_D = 0.67$ V. Given that the work function of the

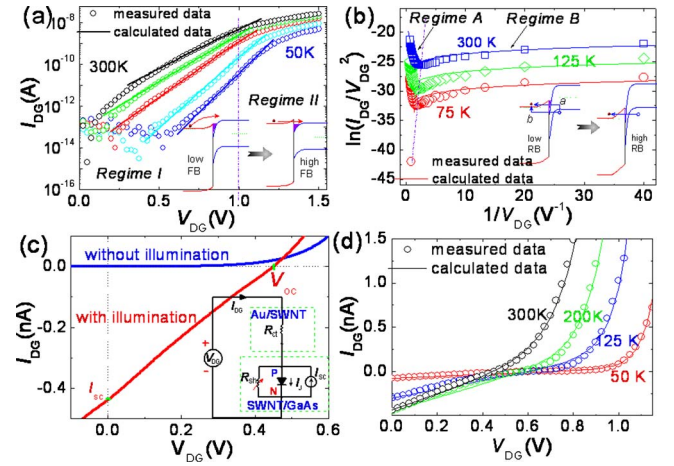


FIG. 3. (Color online) (a) Logarithmic plot of the measured (symbols) and calculated (lines) temperature-dependent I_{DG} vs V_{DG} . Inset: schematic energy band diagrams under low and high FB, respectively. (b) Measured (symbols) and calculated (lines) $\ln(I_{DG}/V_{DG}^2)$ vs $1/V_{DG}$ under RB at 75, 125, and 300 K, respectively. For clarity, the curves for 125 and 75 K are shifted downwards by 2.5 and 5 units, respectively. Inset: schematic energy band diagrams under low and high RB, respectively. (c) I_{DG} – V_{DG} with and without illumination at 300 K. I_{sc} and V_{oc} represent the short-circuit current and open-circuit voltage, respectively. Inset: dc equivalent circuit of the SWNT/GaAs p-n heterojunction with illumination. R_{ct} and R_{sh} are the Au/SWNT contact and shunt resistances, respectively. I_{sc} is a constant current source. (d) Measured (symbols) and calculated (lines) data under illumination at 50, 125, 200, and 300 K, respectively.

n-type GaAs is 4.07 eV,¹⁸ the work function of SWNT equals 4.74 eV. It indicates that the Fermi level of the SWNT is ~ 70 meV below the midgap,¹⁷ consistent with the ambipolar conduction with stronger p-type conductance [Fig. 1(b)]. Moreover, V_D is the sum of the partial built-in potentials in the GaAs (V_{D1}) and SWNT (V_{D2}), i.e., $V_D = V_{D1} + V_{D2}$, where $V_{D1}/V_{D2} = (N_A\epsilon_2)/(N_D\epsilon_1)$.¹⁶ The relative permittivity of GaAs is $\epsilon_1 = 12.85$.¹⁹ The doping concentration of the n-type GaAs is $N_D \approx 1.26 \times 10^6$ electrons/cm. The hole doping concentration in the SWNT due to oxygen adsorption in air can be $N_A \approx 6 \times 10^5$ holes/cm, which is estimated from a CNT diode structure.²⁰ The relative permittivity of the our SWNT can be estimated to be $\epsilon_2 = 3.4$.^{21,22} As a result, $V_{D2} \approx 7.4 V_{D1}$, i.e., the partial built-in potentials in the SWNT and GaAs are about 0.59 and 0.08 V, respectively. As larger portion of the built-in potential occurs in the SWNT, the band bending in the SWNT is much more severe than that in the GaAs. Since the Fermi level of the GaAs is close to its CB,²³ the energy barrier for electron transport from the GaAs to SWNT in the absence of bias voltage is $\phi \approx q(V_D - \Delta E_c) = 0.37$ eV [Fig. 2(d)]. On the other hand, the activation energy in the absence of electric field is extrapolated at $V_{DG} = 0$ to be ~ 0.27 eV from the $E_a - \sqrt{V_{DG}}$ relation in regime I of Fig. 2(c).²⁴ The deviation could result from the one-dimensional (1D) nature of SWNTs, whose depletion width W_{CNT} is extremely sensitive to the doping concentration N_A , $W_{CNT} \propto \exp(N_A^{-1})$.²⁵

The logarithmic plot of calculated and measured I_{DG} – V_{DG} curves is presented in Fig. 3(a). It is noted that the calculated curves fit the experimental ones in regime I, but not in regime II, indicating that a different mechanism dominates the carrier transport in regime II. Under high FB (regime II), the CB of the GaAs is nearly as high as that of the SWNT [see the inset of Fig. 3(a)] so that electrons from the

GaAs tunneling through the spike barrier dominate the current. Thus, V_{DG} is inefficient in varying the current. The slope of $\log I_{DG}-V_{DG}$ under RB [Fig. 2(b)] shows weak temperature-dependence, suggesting the tunneling mechanism. Zeidenbergs and Anderson²⁶ proposed that the tunneling could occur through two possible processes, as shown in the inset of Fig. 3(b) (path a and b).

Interestingly, the $I-V$ characteristics under RB fit the electron transport through an arbitrary molecular-scale junction, implying that the 1D SWNT plays a critical role. Within the Simmons²⁷ approximation, the $I-V$ relation of an arbitrary molecular-scale tunnel junction is

$$I = \frac{q\alpha}{4\pi^2\hbar d^2} \left\{ \left(\phi - \frac{qV}{2} \right) \exp \left(-\frac{2d\sqrt{2m_e}}{\hbar} \sqrt{\phi - \frac{qV}{2}} \right) - \left(\phi + \frac{qV}{2} \right) \exp \left(-\frac{2d\sqrt{2m_e}}{\hbar} \sqrt{\phi + \frac{qV}{2}} \right) \right\}, \quad (2)$$

where α is the molecular junction area, d is the barrier width, m_e is the electron effective mass, ϕ is the barrier height, and \hbar is the reduced Planck constant. For a rectangular tunneling barrier (low bias), Eq. (2) is reduced to $\ln(I/V^2) \propto \ln(1/V) - 2d\sqrt{2m_e}\phi/\hbar$. In contrast, for a triangular tunneling barrier (high bias), Eq. (2) can be simplified as $\ln(I/V^2) \propto (1/V)4d\sqrt{2m_e}\phi^3/3\hbar q$.²⁸ Figure 3(b) shows the plots of $\ln(I_{DG}/V_{DG}^2)$ versus $1/V_{DG}$ under RB at 75, 125, and 300 K, respectively. The curves consist of linear (regime A) and nonlinear (regime B) regimes. From the plot, one can differentiate the transport governed by direct tunneling from Fowler–Nordheim (F–N) tunneling. In regime A, the curves are described by $\ln(I_{DG}/V_{DG}^2) \propto C_1(1/V_{DG})$, while, the curves fit $\ln(I_{DG}/V_{DG}^2) \propto \ln(1/V_{DG}) + C_2$ in regime B (C_1 and C_2 are constant). It thus suggests that the transport mechanism has experienced a transition from the direct tunneling to F–N tunneling [see the inset of Fig. 3(b)]. Under a low RB, the tunneling junction consists of the spike barrier (on the GaAs side) and the SWNT band gap (on the SWNT side). The relation between $\ln(I_{DG}/V_{DG}^2)$ and $1/V_{DG}$ (regime B) suggests that the transport is dominated by the direct tunneling (through a rectangular barrier). Nevertheless, under the high RB, the spike barrier on the GaAs side could be much thicker than the barrier on the SWNT side because the energy band bending in the SWNT is much more severe than that in the GaAs. In this case, the tunneling through the spike barrier may dominate the transport, consistent with the suggestion of F–N tunneling (through a triangular barrier) in regime A.

The PV response of the heterojunction is shown in Figs. 3(c) and 3(d). At 300 K, the short-circuit current I_{sc} and open-circuit voltage V_{oc} are 440 pA and 450 mV, respectively [Fig. 3(c)]. The PV effect can be modeled as a constant current source I_{sc} , a shunt resistor R_{sh} , and a series resistor R_{ct} , as shown in the inset.^{29,30} Then the $I_{DG}-V_{DG}$ characteristic under illumination is given by

$$I_{DG} = \frac{(I_j - I_{sc})R_{sh} + V_{DG}}{R_{ct} + R_{sh}}, \quad (3)$$

where I_j is the FB heterojunction current described by Eq. (1). As shown in Fig. 3(d), the calculated $I_{DG}-V_{DG}$ curves based on Eq. (3) fit reasonably well to the measured results

(See the supplementary information for the details of calculation).

In conclusion, the conduction mechanisms of a SWNT/GaAs p-n heterojunction have been studied systematically. At a low-FB, electron thermionic emission over the energy barrier between the CBs of the SWNT and GaAs dominates the carrier transport. While, electron tunneling through the spike barrier due to the CB discontinuity determines the current at a high-FB. In contrast, under a high-RB, F–N tunneling through a molecular junction is the dominant transport mechanism. While, at a low-RB, hole tunneling through the interband states mainly contributes the current. Owing to the one dimensionality of the nanotube, the tunneling current plays a significant role under various bias conditions. Within the aforementioned framework, the PV response of the SWNT/GaAs heterojunction is quantitatively modeled.

This work was supported by MOE AcRF Tier 2 Funding (Grant Nos. ARC 17/07 and T207B1203). One of the authors (H.L.) would like to thank Singapore Millennium Foundation for financial support.

- ¹K. Lee, Z. Wu, Z. Chen, F. Ren, S. J. Pearton, and A. G. Rinzier, *Nano Lett.* **4**, 911 (2004).
- ²T. Kawano, D. Christensen, S. Chen, C. Y. Cho, and L. Lin, *Appl. Phys. Lett.* **89**, 163510 (2006).
- ³D. A. Straus, M. Tzolov, T.-F. Kuo, A. Yin, and J. M. Xu, *IET Circuits Devices Syst.* **1**, 200 (2007).
- ⁴M. S. Purewal, B. H. Hong, A. Ravi, B. Chandra, J. Hone, and P. Kim, *Phys. Rev. Lett.* **98**, 186808 (2007).
- ⁵T. Dürkop, S. A. Getty, E. Cobas, and M. S. Fuhrer, *Nano Lett.* **4**, 35 (2004).
- ⁶M. B. Živanov and Lj. D. Živanov, Proceedings of the 20th International Conference on Microelectronics (MIEL'95), Niš, Serbia, 12–14 September 1995 (unpublished), Vol. 1.
- ⁷H. Kataura, Y. Kumazawa, Y. Maniwa, Y. Ohtsuka, R. Sen, S. Suzuki, and Y. Achiba, *Carbon* **38**, 1691 (2000).
- ⁸C. L. Cheung, A. Kurtz, H. Park, and C. M. Lieber, *J. Phys. Chem. B* **106**, 2429 (2002).
- ⁹P. L. McEuen, M. S. Fuhrer, and H. Park, *IEEE Trans. Nanotechnol.* **1**, 78 (2002).
- ¹⁰C.-W. Liang and S. Roth, *Nano Lett.* **8**, 1809 (2008).
- ¹¹J. Li, Q. Zhang, D. Yang, and J. Tian, *Carbon* **42**, 2263 (2004).
- ¹²J. Li, Q. Zhang, N. Peng, and Q. Zhu, *Appl. Phys. Lett.* **86**, 153116 (2005).
- ¹³A. R. Riben and D. L. Feucht, *Solid-State Electron.* **9**, 1055 (1966).
- ¹⁴Y.-F. Chen and M. S. Fuhrer, *Nano Lett.* **6**, 2158 (2006).
- ¹⁵J. Appenzeller, M. Radosavljević, J. Knoch, and Ph. Avouris, *Phys. Rev. Lett.* **92**, 048301 (2004).
- ¹⁶R. L. Anderson, *Solid-State Electron.* **5**, 341 (1962).
- ¹⁷B. Shan and K. Cho, *Phys. Rev. Lett.* **94**, 236602 (2005).
- ¹⁸G. W. Gobeli and F. G. Allen, *Phys. Rev.* **137**, A245 (1965).
- ¹⁹J. S. Blakemore, *J. Appl. Phys.* **53**, R123 (1982).
- ²⁰C. Zhou, J. Kong, E. Yenilmez, and H. Dai, *Science* **290**, 1552 (2000).
- ²¹L. X. Benedict, S. G. Louie, and M. L. Cohen, *Phys. Rev. B* **52**, 8541 (1995).
- ²²R. Krupke, F. Hennrich, H. V. Löhneysen, and M. M. Kappes, *Science* **301**, 344 (2003).
- ²³S. M. Sze, *Physics of Semiconductor Devices* (Wiley, New York, 1981).
- ²⁴R. Martel, V. Derycke, C. Lavoie, J. Appenzeller, K. K. Chan, J. Tersoff, and Ph. Avouris, *Phys. Rev. Lett.* **87**, 256805 (2001).
- ²⁵F. Léonard and J. Tersoff, *Phys. Rev. Lett.* **83**, 5174 (1999).
- ²⁶G. Zeidenbergs and R. L. Anderson, *Solid-State Electron.* **10**, 113 (1967).
- ²⁷J. G. Simmons, *J. Appl. Phys.* **34**, 1793 (1963).
- ²⁸J. M. Beebe, B. S. Kim, J. W. Gadzuk, C. D. Frisbie, and J. G. Kushmerick, *Phys. Rev. Lett.* **97**, 026801 (2006).
- ²⁹M. B. Prince, *J. Appl. Phys.* **26**, 534 (1955).
- ³⁰See supplementary material at <http://dx.doi.org/10.1063/1.3293452> for the details of sample fabrication and data fitting.